Regularized Ultrasound Phantom-Free Local Attenuation Coefficient Slope (ACS) Imaging in Homogeneous and Heterogeneous Tissues

Iman Rafati, François Destrempes, Ladan Yazdani, Marc Gesnik, An Tang, and Guy Cloutier, *Senior Member, IEEE*

***Abstract*— Attenuation maps or measurements based on the local attenuation coefficient slope (ACS) in quantitative ultrasound (QUS) have shown potential for the diagnosis of liver steatosis. In liver cancers, tissue abnormalities and tumors detected using ACS are also of interest to provide new image contrast to clinicians. Current phantom-based approaches have the limitation of assuming a comparable speed of sound between the reference phantom and insonified tissues. Moreover, these methods present the inconvenience for operators to acquire data on phantoms and patients. The main goal was to alleviate these drawbacks by proposing a methodology for constructing phantom-free regularized (PF-R) local ACS maps and investigate the performance in both homogeneous and heterogeneous media. The proposed method was tested on two tissue-mimicking media with different ACS constructed as homogeneous phantoms, side-by-side and top-to-bottom phantoms, and inclusion phantoms with different attenuations. Moreover, an in vivo proof-of-concept was performed on healthy, steatotic, and cancerous human liver datasets. Modifications brought to previous works include: 1) a linear interpolation of the power spectrum in the log scale; 2) the relaxation of the underlying hypothesis on the diffraction factor; 3) a generalization to nonhomogeneous local ACS; and 4) an adaptive restriction of frequencies to a more reliable range than the usable frequency range. Regularization was formulated as a generalized least absolute shrinkage and selection operator (LASSO), and a variant of the Bayesian information criterion (BIC) was applied to estimate the Lagrangian multiplier on the LASSO constraint. In addition, we evaluated the proposed algorithm when applying median filtering before and after regularization. Tests conducted showed that the PF-R yielded robust results in all tested conditions, suggesting potential for additional validation as a diagnosis method.**

***Index Terms*— Compression wave attenuation imaging, local attenuation coefficient slope (ACS), quantitative ultrasound (QUS), regularization, system-independent tissue characterization, ultrasound (US) attenuation coefficient (AC) estimation.**

I. Introduction

HEPATOCELLULAR carcinoma (HCC) is responsible for between 85% and 90% of primary liver cancers [1], [2], and they are the fourth most common cause of cancer-related mortality [3]. The mortality rate of HCC is increasing by 3% per year due to late diagnosis [4], [5]. Early detection of HCC is critical to increase the opportunity for curative treatment and to improve survival. Ultrasound (US) is used clinically for HCC surveillance due to its wide availability, cost-effectiveness, and noninvasiveness compared to other methods, such as biopsy, magnetic resonance imaging (MRI), and computed tomography [6], [7]. However, US has a lower sensitivity [8], [9] for detecting focal lesions, especially in the presence of concomitant liver steatosis, fibrosis, or cirrhosis [10], [11]. To overcome this limitation, one may extract additional information from US not available on the B-mode, Doppler, or elastography images, such as attenuation coefficient slope (ACS) maps estimated using quantitative US (QUS) [12], [13], [14], [15].

QUS attenuation has been used in several clinical studies to assess the degree of liver injury and specifically of liver steatosis [16], [17], [18], [19]. This feature is used by radiologists to detect and assess the severity of the fatty liver disease. The accumulation of fat in the liver can progress to fibrosis, cirrhosis, and eventually to HCC [20]. The presence of moderate-to-severe liver steatosis constitutes a diagnostic challenge as it may obscure tumors in attenuated portions of the liver [21]. US attenuation is more economical than MRI for screening and surveillance [22], mainly due to clinical

Manuscript received 28 September 2022; accepted 24 October 2022. Date of publication 1 November 2022; date of current version 28 November 2022. *(Corresponding author: Guy Cloutier.)*

This work was supported in part by the Natural Sciences and Engineering Research Council of Canada under Grant ALLRP-561770-21, in part by the Canadian Institutes of Health Research under Grant 389385, and in part by the Oncotech consortium (Oncopole, Medteq, Transmedtech, Cancer Research Society, Fonds de Recherche Santé du Québec, and Siemens Healthcare) under Grant 293741.

This work involved human subjects or animals in its research. Approval of all ethical and experimental procedures and protocols was granted by the Institutional Review Board on Ethics of the University of Montreal Hospital Research Center.

Iman Rafati and Ladan Yazdani are with the Laboratory of Biorheology and Medical Ultrasonics, University of Montreal Hospital Research Center, Montreal, QC H2L 2W5, Canada, and also with the Institute of Biomedical Engineering, University of Montreal, Montreal, QC H3C 3J7, Canada.

François Destrempes is with the Laboratory of Biorheology and Medical Ultrasonics, University of Montreal Hospital Research Center, Montreal, QC H2L 2W5, Canada.

Marc Gesnik was with the Laboratory of Biorheology and Medical Ultrasonics, University of Montreal Hospital Research Center, Montreal, QC H2L 2W5, Canada. He is now with Iconeus, 75014 Paris, France.

An Tang is with the Clinical Laboratory of Image Processing, University of Montreal Hospital Research Center, Montreal, QC H2L 2W5, Canada, and also with the Department of Radiology, Radio-Oncology and Nuclear Medicine, University of Montreal, Montreal QC H3C 3J7, Canada.

Guy Cloutier is with the Laboratory of Biorheology and Medical Ultrasonics, University of Montreal Hospital Research Center, Montreal, QC H2L 2W5, Canada, and also with the Department of Radiology, Radio-Oncology and Nuclear Medicine, and Institute of Biomedical Engineering, University of Montreal, Montreal QC H3C 3J7, Canada (e-mail: guy.cloutier@umontreal.ca).

Digital Object Identifier 10.1109/TUFFC.2022.3218920

successes of the controlled attenuation parameter (CAP) to grade liver steatosis [17]. Notice that no images are produced with the CAP parameter.

The loss of ultrasonic energy when an acoustic wave propagates through soft tissues is referred to as ultrasonic attenuation [23]; it is due to scattering and absorption (conversion of ultrasonic to thermal energy) [24]. Clinicians performing conventional B-mode assessment can detect attenuation qualitatively [25], [26]. The attenuation is related to the interaction of propagating compression waves within tissues, resulting in a decrease in the echo intensity along the wave propagation path, loss in B-mode detectable image features, and shadowing [27]. While attenuation was traditionally considered an imaging artifact, it can be leveraged as a specific feature with diagnostic value [12]. Indeed, attenuation depends on the underlying nature and structure of a tissue [28]. To clarify this concept, several parameters can be defined as attenuation in the US literature. The total attenuation coefficient (total AC) is defined as the attenuation-to-depth ratio, which depends on intervening tissues along the whole propagation path [12], [23]. The local AC can be defined as the partial derivative of attenuation with respect to depth, which depends on tissues at a given position [29]. By assuming a linear dependency on frequency, the slope of AC (ACS) is most often used in the literature [23], [25], [30], [31], [32], [33], [34], [35].

Constructing attenuation images is an approach that can be used to assist in the detection of lesions and abnormalities of the liver. Popular methods to estimate ACS using clinical US scanners in backscattering mode [15], [36], [37] are the spectral difference [38], [39] and spectral shift [40] methods. Both spectral-based approaches estimate the local ACS (dB cm^{-1} MHz^{-1}) inside a prespecified region of interest (ROI) [23]. The spectral difference method uses the reduction of the echo signal power with depth to determine the local AC, whereas the spectral shift method utilizes the downshift in the center frequency of the backscatter echo with depth to obtain frequency-dependent attenuation [15], [40]. The spectral log-difference (SLD) method [23], [34] and a hybrid method [32] are two other variants of these techniques.

With these methods, scattering properties (i.e., the backscatter coefficient) are assumed to be constant over depth within the ROI. Furthermore, to compensate for the US beam diffraction and other system-dependent effects, such as gain, filtering, and the piezoelectric acoustical transfer function at emission and reception, echo signals from a reference phantom whose acoustic properties are known (through calibration) are required [41]. It is worth mentioning that these echo signals must be acquired using the same equipment and system settings as the clinical exam, and the speed of sound of the reference phantom needs to be close to the one of the acquired tissues' samples [12], [23]. The ratio of power spectra from tissues' samples and reference phantom, at two different depths, yields the local AC of the scanned organ at the frequency and depth of interest [14]. The availability of a well-calibrated reference phantom can, thus, be considered a limitation of these methods [42].

Recent studies proposed system-independent methods as an alternative for estimating local attenuation without the need for a reference phantom [42], [43]. This strategy cancels system-dependent effects using spectral normalization in adjacent frequency components and is known as the reference frequency method (RFM). This method has some limitations, such as the need for a predefined frequency range and a large computing window (CW) (a square with side lengths of 2.5 cm), which make the use of this method limited to the case of homogeneous media preventing cancer lesions detection. Thus, a method is needed to overcome these limitations to provide parametric maps for cancer diagnosis purposes. In our preliminary study [43], reconstructions of attenuation images using a system-independent method showed promising results close to the ground truth (through-transmission substitution method) [36], in the case of homogeneous and side-by-side phantoms. This study provides additional validations with top-to-bottom phantoms and is also focusing on differentiating lesions with different attenuation and geometrical properties than surrounding tissues. More specifically, we present the development and validation of a phantom-free attenuation mapping method with parametric regularization to reduce image artifacts for applications in liver steatosis grading, and liver cancer detection and characterization.

The remaining part of this article is organized as follows. Section II introduces the theoretical framework and governing equations for estimating the ACS. Section III describes experimental configurations and acquisitions. Section IV presents results acquired on phantoms with the phantom-free (PF) and the SLD methods before and after regularization (R). Section V discusses advantages and future directions, followed by Section VI on conclusions.

II. Theoretical Framework

The ACS can be evaluated using a methodology that involves radio frequency (RF) data acquisition without the need of acquiring RF signals from a reference phantom. The method is based on spectra normalization at different frequencies [43]. Specific contributions are: 1) a linear interpolation of the power spectrum in the log scale; 2) the relaxation of the underlying hypothesis on the diffraction factor within an ROI; and 3) a generalization to nonhomogeneous local ACS. Moreover, we provide a regularized local attenuation map based on the selected ROI.

A. Power Spectrum Modeling

Within the ROI, a CW centered at depth z (cm) (the lateral position is dropped in the equations for simplicity of notation) is considered. The power spectrum $S(f, z)$ at depth z of backscattered RF signals in the time domain ($x_z(t)$) after removing the time gain compensation (TGC) of the US system, which was automatically recorded as a function of depth, can be computed as in the following equation:

$$S(f, z) = \left\langle |X_z(f)|^2 \right\rangle \tag{1}$$

where f(MHz) is the frequency, $X_z(f)$ is the Fourier transform of $x_z(t)$ over a scan line centered at z, $|X_z(f)|$ denotes the complex modulus of $X_z(f)$, and $\langle - \rangle$ represents the averaging operator over scan lines. Power spectra were estimated by computing Fourier transforms of RF signals after applying a rectangular window with zero padding and averaging over 25 adjacent scan lines (see [44]).

The power spectrum can be modeled as a function of the US frequency and depth according to previous studies [31], [42] in the form of the following equation:

$$S(f_i, z_k) = G(f_i)D(f_i, z_k)\mathrm{BSC}(f_i, z_k)A(f_i, z_k) \tag{2}$$

where S is the power spectrum as a function of frequency f_i (i is the frequency component index) and depth z_k (k is the depth index), G is the transducer's response in transmit and receive modes at a given frequency, D represents combined effects of focusing, beamforming, and beam diffraction, BSC (cm^{-1}. sr^{-1}) is the backscatter coefficient, and A is the attenuation component, which is assumed to be in the form $\exp(-4\alpha_{\mathrm{total},\,z_k} z_k f_i)$, where $\alpha_{\mathrm{total},\,z_k}$ (Nepers cm^{-1} MHz^{-1}) is the total ACS at depth z_k, assuming a linear dependency with frequency.

The first modification to [43] was to consider a Gaussian fit in the log scale to power spectra for improving the robustness of ACS maps. Next, according to [42], the power ratio $\mathrm{RS}(f_i, z_k)$ (no unit) between adjacent frequency components $S(f_i, z_k)$ and $S(f_{i-1}, z_k)$ can be expressed as

$$\begin{aligned}\mathrm{RS}(f_i, z_k) &= \frac{S(f_i, z_k)}{S(f_{i-1}, z_k)} \\ &= \frac{G(f_i)D(f_i, z_k)\mathrm{BSC}(f_i, z_k)A(f_i, z_k)}{G(f_{i-1})D(f_{i-1}, z_k)\mathrm{BSC}(f_{i-1}, z_k)A(f_{i-1}, z_k)}.\end{aligned} \tag{3}$$

We assume that beamforming and diffraction effects between two adjacent frequencies f_i and f_{i-1} are related linearly in the form $D(f_i, z_k) = c_i D(f_{i-1}, z_k)$, where the unknown constant of proportionality c_i depends only on frequencies f_i and f_{i-1}. With this assumption, (3) simplifies to

$$\mathrm{RS}(f_i, z_k) = \frac{G(f_i)\, c_i \mathrm{BSC}(f_i, z_k)A(f_i, z_k)}{G(f_{i-1})\mathrm{BSC}(f_{i-1}, z_k)A(f_{i-1}, z_k)}. \tag{4}$$

To obtain a linear equation, the natural logarithm is applied to (4) yielding

$$\begin{aligned}&\log \mathrm{RS}(f_i, z_k) \\ &\quad = \log G(f_i) - \log G(f_{i-1}) + \log \mathrm{BSC}(f_i, z_k) \\ &\qquad - \log \mathrm{BSC}(f_{i-1}, z_k) - 4\alpha_{\mathrm{total},\,z_k} z_k (f_i - f_{i-1}) + \log c_i.\end{aligned} \tag{5}$$

By taking the difference in the expression $\log \mathrm{RS}(f_i, z_k)$ at two different depths z_k and z_r yet, at the same frequencies, the terms for transmit and receive transducer's responses and the backscatter coefficient can be canceled from (5) by assuming that $\mathrm{BSC}(f_i, z_k) = \mathrm{BSC}(f_i, z_r)$. Furthermore, upon considering the relation $\alpha_{\mathrm{total},\,z_k} z_k = \alpha_{\mathrm{total},\,z_r} z_r + \alpha_{\mathrm{local},\,z}(z_k - z_r)$, where $\alpha_{\mathrm{local},\,z}$ is the local ACS for a CW centered at depth z, (5) yields after simplifications

$$\begin{aligned}&\log \mathrm{RS}(f_i, z_k) - \log \mathrm{RS}(f_i, z_r) \\ &\qquad = -4\alpha_{\mathrm{local},\,z}(z_k - z_r)(f_i - f_{i-1}).\end{aligned} \tag{6}$$

To lighten the notation in (6), the normalized ratio of power spectra $\mathrm{RS}_{\mathrm{nor}}(f_i, z_k, z_r)$ is defined as

$$\mathrm{RS}_{\mathrm{nor}}(f_i, z_k, z_r) = \mathrm{RS}(f_i, z_k)/\mathrm{RS}(f_i, z_r). \tag{7}$$

With this definition, (6) now reads as

$$\log \mathrm{RS}_{\mathrm{nor}}(f_i, z_k, z_r) = -4\alpha_{\mathrm{local},\,z}(z_k - z_r)(f_i - f_{i-1}). \tag{8}$$

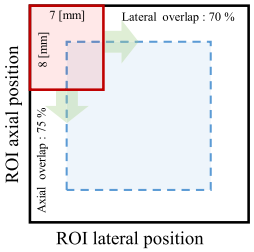

Fig. 1. Schematic of an ROI (black box), one CW (red box), and center positions of CWs included in the blue box in dashed line. Overlaps of CWs in lateral and axial positions are 70% and 75%, respectively.

Another modification to Gong et al. [42] was restricting the frequency range within the usable frequency range (UFR) as follows. First, the log-power spectrum ratio at a given frequency f as a function of depth z was approximated by a linear function $-a(f)z + b(f)$ using the line fitting described in Section II-B. The frequency f_* at which the y-intercept $b(f)$ is maximal was selected. This procedure yielded the frequency with the overall maximal power spectrum. The quantity $a(f_*)$ represents an approximate estimate of the local ACS at frequency f_* [see (2)]. The frequency range was then restricted to those frequencies f_i for which the ratio [obtained from (8)] lies within 25% of $a(f_*)$

$$\begin{aligned}(1 - 0.25)a(f_*) &\le \frac{\log \mathrm{RS}_{\mathrm{nor}}(f_i, z_k, z_r)}{-4(z_k - z_r)(f_i - f_{i-1})} \\ &\le (1 + 0.25)a(f_*).\end{aligned} \tag{9}$$

The final local ACS estimate was obtained by performing a linear regression on (8) within the obtained restricted frequency range, which is ROI-dependent. Based on data inspection, the frequency range turned out to be continuous. This is a new alternative to the procedure that was proposed by Gong et al. [42], where the frequency range was selected by considering the top of the histogram of the estimated parameter. The new method was applied to small CWs within the ROI to obtain a local ACS map, as shown in Fig. 1. In this illustrative example of an arbitrary ROI, the height and width of CWs were approximately 8 mm (10 pulse lengths) × 7 mm (25 scan lines), respectively, with 70% and 75% overlapping in lateral and axial directions, respectively. These window dimensions and overlaps remained constant for all results presented in this study.

B. Line-Fitting Method

The purpose of this method is to find a linear relation between the depth (z) and the logarithm of the power spectra ratio ($\log \mathrm{RS}$). Under the random sample consensus (RANSAC) approach, outlier values (i.e., points too far away from the regression line) in experimental data are removed from the line fitting [45]. The second issue is the boundary between two different media in the tissues' samples. In presence of two media, there might be two lines with different slopes. It should be mentioned that points used for the line-fitting method are denoted as inliers in the RANSAC approach. The following algorithm, as displayed in Fig. 2, was used to find the slope based on the number of points per line (inliers), after outliers' rejection.

In Fig. 2(a), we considered three possible cases to find inliers. In the first case, there is no change in the

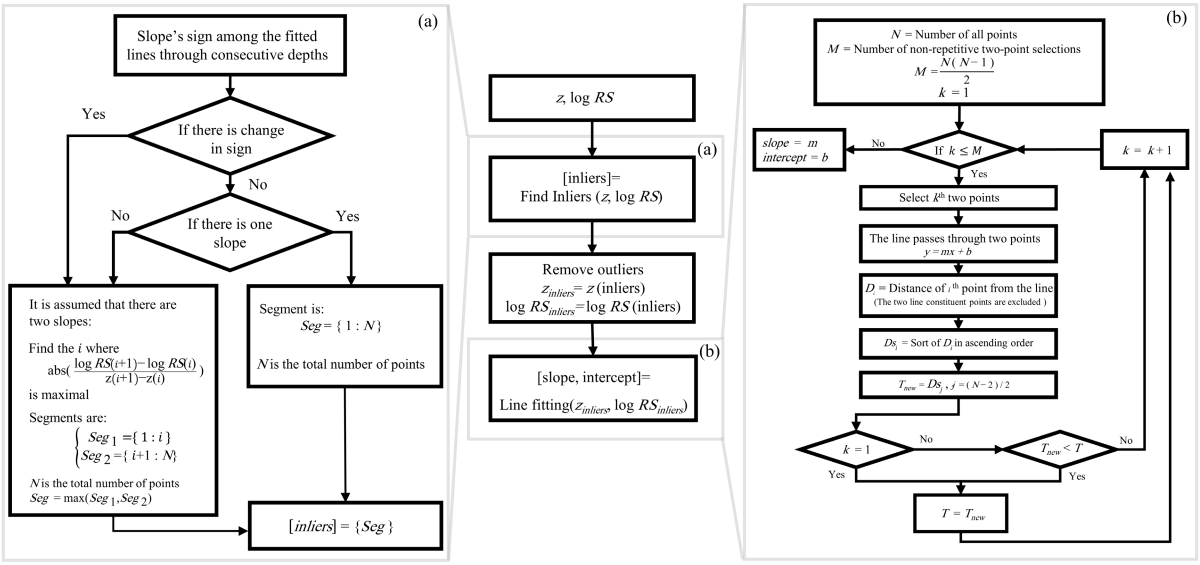

Fig. 2. Algorithm for approximate estimation of the local ACS at a given frequency by line fitting the logarithm of power spectra ratio (log RS) at a given frequency as a function of depth z. (a) Algorithm consists of finding inliers (i.e., the points to be considered for line fitting). (b) Slope of the fit line on the inliers based on a RANSAC approach.

slope's sign among fit lines through consecutive depths (z_k). If there is a single slope, which represents the case of a homogenous sample with a single medium, then all points are considered for line fitting. If there are two different slopes, but with the same sign (second case), we assume a piecewise linear curve consisting of two segments. We chose the largest slope in absolute value, i.e., argmax abs$\{(\log \mathrm{RS}(i+1) - \log \mathrm{RS}(i))/(z(i+1) - z(i))\}$, to determine the location of the change in segments. Inliers are then the points belonging to the segment comprising the most points. In the case of a tie, the first segment was selected as a set of inliers. In the third case, there is a change in the slope's sign among fit lines through consecutive depths. As in the second case, inliers are then the points of the segment comprising the most points (taking the segment occurring first in the case of a tie).

In Fig. 2(b), RANSAC line fitting was applied to selected inliers, as in [45] and [46]. Two modifications were brought to RANSAC's original formulation. The first one is to examine all combinations of two points instead of selecting randomly two points, which is convenient due to the limited number of points in this context (less than ten points based on the size of segments; see Fig. 2). As for the second modification, instead of considering an acceptable number of inliers based on a fixed threshold and choosing a pair of points with the maximal number of inliers, the selection of pairs of points was based on both the number of inliers and the proximity of other points to the fit line using no fixed threshold. Therefore, all combinations of two points (i and j) among inliers were being considered. An initial threshold (T_{new}) was set such that half of the remaining points were within the threshold. As a result, at least half of the points (including the pair that defined the line) have been considered inliers. This threshold was updated by iterations on all combinations of two points [M in Fig. 2(b)]. Finally, the line with the lowest threshold that contained more than half of the points was selected as the result of the line fitting.

C. Regularization

1) Linear Regression Formulation and Data Fidelity Term: In the context of the regularization of parametric maps in which each pixel represents a CW, a linear regression formulation of the following form can be defined:

$$y_r = X_r \beta_r + \varepsilon_r \tag{10}$$

where r denotes a CW and $y_r = (y_r(f_i))_{i=1}^{N_{\mathrm{Freq}}}$ represents the observed spectral data expressed at each frequency f_i (MHz) of the discretized UFR. Moreover, the matrix X_r represents the model's predictors, while β_r corresponds to the vector of regression coefficients. Here, ε_r is the residual noise, assumed to be zero mean with variance σ^2. Assuming independent identically distributed residual noise over all CWs, one is led to the following data fidelity term (i.e., the residual "res," which expresses the least mean squared error (LMSE) between the observed data and the fit model):

$$\mathrm{res}(y, \beta) = \frac{1}{2} \sum_{r=1}^{N_{\mathrm{CW}}} w_r^2 \| y_r - X_r \beta_r \|_2^2 \tag{11}$$

where N_{CW} is the number of CWs for parameters estimation, w_r is a positive weight assigned to the CW indexed by r, and $\| - \|_2$ denotes the ℓ_2-norm. The likelihood $L(y|\beta, \sigma^2)$ is then of the form: $\exp(-\mathrm{res}(y, \beta)/\sigma^2)$.

The data fidelity term is detailed as follows in the case of the proposed phantom-free local attenuation model, while this term in the case of the SLD model used for comparison is described in Appendixes. The observed spectral data are on the left-hand side of (8) and are then given by (viewed as a vector)

$$y_r = (\log \mathrm{RS}_{\mathrm{nor}}(f_i, z_k, z_k))_{i=1}^{N_{\mathrm{Freq}}}. \tag{12a}$$

The predictors' matrix (a vector in this case) and the regression coefficient (a scalar in this case) are then of the form

$$X_r = (-4(z_k - z_n)(f_i - f_{i-1}))_{i=1}^{N_{\mathrm{Freq}}}, \quad \text{and} \tag{12b}$$

$$\beta_r = \alpha_{r,\mathrm{local}}. \tag{12c}$$

To determine the weights w_r appearing in (11), we first solved this LMSE problem with initial weights set to 1. Then, Fisher tests [47] were applied to each underlying linear regression, and the resulting p-values were adopted as weights in that equation. In the case of a numerically vanishing p-value, it was replaced by the small quantity 10^{-5}.

2) Regularization Term: In the least absolute shrinkage and selection operator (LASSO) framework, the ℓ_1-norm regularization term imposed on linear regression coefficients β is of the form [48]

$$\mathrm{reg}_1(\beta, \lambda) = \lambda \sum_{r=1}^{N_{\mathrm{CW}}} \sum_{m=1}^{d} \sum_{s \in N(r)} \left| \beta_{r,m} - \beta_{s,m} \right| \tag{13a}$$

where λ is the Lagrange multiplier (LM), which weights the strength of the constraint with respect to the data fidelity term, $d = 1$ for the phantom-free attenuation method or $d = 2$ for the SLD attenuation model (see Appendix A), where d is the number of model parameters being estimated, and $N(r)$ denotes the set of previous (adjacent) CWs to a given CW, one along the axial direction and the other along the lateral direction. This constraint favors naturally identical regression coefficients on adjacent CWs and, hence, causes CWs to get fused (i.e., to share the same regression coefficients). In the LASSO formalism, (13a) may be recast in the form

$$\mathrm{reg}_1(\beta, \lambda) = \lambda \| D\beta \|_1 \tag{13b}$$

where D represents the constraint matrix, $\beta = (\beta_r)$ is the vector of regression coefficients, and $|| - ||_1$ denotes the ℓ_1-norm. However, to address adjacent CWs belonging to different tissues, the links between adjacent CWs were assessed based on Nakagami goodness-of-fit tests along axial and lateral directions. Namely, the Kolmogorov–Smirnov goodness-of-fit test [49] was applied to the data corresponding to the US echo envelope encompassing the two adjacent CWs with Nakagami distribution [50] as the underlying statistical model. When the goodness-of-fit failed between two adjacent CWs (with a confidence level of 0.1), the corresponding link was removed in the constraint matrix D (i.e., the corresponding entry was set to 0).

The corresponding prior on regression coefficients is of the form: $\pi(\beta|\lambda) = \exp(-\mathrm{reg}_1(\beta, \lambda))$. For a given LM value λ, one seeks the vector of coefficients $\hat{\beta}(\lambda)$ that minimize the corresponding energy functional

$$\mathrm{res}(\mathrm{y}, \beta) + \mathrm{reg}_1(\beta, \lambda). \tag{14}$$

Notice that, in principle, the LASSO constraint favors sparsity in differences of regression coefficients, even more so than the ℓ_2-norm regularization constraint. From Tibshirani and Taylor [48], the curve expressing $\mathrm{res}(\mathrm{y}\ \hat{\beta}(\lambda)) + \mathrm{reg}(\hat{\beta}(\lambda), \lambda)$ as a function of λ can be described as a piecewise linear curve based on finitely many values of λ, which are obtained efficiently with the path algorithm [48]. In this work, we used our own implementation of the path algorithm on MATLAB (version R2018a, The MathWorks, Natick, MA, USA).

3) Model's Selection: The Bayesian information criterion (BIC) [51] yields, in the LASSO framework [48], the expression

$$\mathrm{BIC}(\lambda) = -2 \log L\left(y|\hat{\beta}(\lambda), \hat{\sigma}^2\right) + C(\lambda) \log N \tag{15}$$

where $L(y|\beta, \sigma^2)$ represents the likelihood of the data based on parameters β and σ^2, $\hat{\beta}(\lambda)$ are the regression coefficients based on the LM λ, $\hat{\sigma}^2$ is the maximum likelihood estimator of the variance σ^2, $N = \dim(y_r)$ is the total sample size in the linear regression problem, and $C(\lambda)$ is the resulting model's complexity. In this work, $C(\lambda)$ was considered as the degrees of freedom df of the solution to (14) times the number of windows within one CW, i.e., the number of depths z_k considered in (12a), since each coefficient β_r intervenes on these distinct windows, albeit with values already fused to a single one. For the SLD attenuation method (see Appendixes), $C(\lambda)$ was taken as df times 2 (i.e., the number of regression coefficients). Thus, having fixed λ, hence $\hat{\beta}_r(\lambda)$, one obtains under stated hypotheses on the observed spectral data noise

$$\hat{\sigma}^2 = \frac{1}{N} \sum_{r=1}^{N_{\mathrm{CW}}} w_r^2 \left\| y_r - X_r \hat{\beta}_r(\lambda) \right\|_2^2. \tag{16}$$

This yields the log-likelihood term for some irrelevant additive constants (const.)

$$\begin{aligned} -2 \log L\left(y|\hat{\beta}(\lambda), \hat{\sigma}^2\right) &= N \log\left(2\pi\hat{\sigma}^2\right) + \frac{1}{\hat{\sigma}^2} \sum_{r=1}^{N_{\mathrm{ROI}}} w_r^2 \left\| y_r - X_r \hat{\beta}_r(\lambda) \right\|_2^2 \\ &= N \log \mathrm{res}\left(y, \hat{\beta}(\lambda)\right) + \mathrm{const.} \end{aligned} \tag{17}$$

According to (15)–(17), the BIC criterion is formulated as choosing the value of λ that minimizes the BIC curve [51]. This is equivalent (as N tends to infinity) to choosing the model (represented here by the fused CWs) for which the data likelihood $\int L(y|\beta)\, \pi(\beta|\lambda)\, d\beta$ is maximal (notice that the larger data likelihood corresponds to the smaller BIC value), where $\pi(\beta|\lambda)$ denotes the prior on regression coefficients implied by the LM.

To favor a greater number of fused CWs within local attenuation maps, we adopted in this work a "strong BIC" criterion [31], [43], which is defined by selecting the largest value of λ for which the condition $\mathrm{BIC}(\lambda) \leq \mathrm{BIC}(0)$ remains valid. This is equivalent to selecting the model that offers the same likelihood as the model without any regularization but with as much regularization as allowed under this condition. Thus, the LM was maximized to yield a BIC value no worse than that of the maximum likelihood.

III. Materials and Methods

A. Phantom Experiments' Description

1) Phantoms Fabrication: Two media were made with a mixture of agar [2% (w/w)], glycerol (10%), and graphite powder (mixture #1, 4.5%; mixture #2, 12%) to investigate the performance of ACS methods in the case of homogeneous and heterogeneous samples [52]. Three categories of phantoms with homogeneous, side-by-side, and top-to-bottom homogeneous media and heterogeneous samples with inclusions were made using these two gel preparations.

a) Homogeneous, side-by-side, and top-to-bottom phantoms: Two homogeneous phantoms were made using mixture #1 (model A) and mixture #2 (model B). A side-by-side phantom (model C) was also made by cutting half of one homogeneous

phantom in its mold after jellifying and pouring the other mixture into the mold. The other orientations of model C (top-to-bottom) in which mixture #2 was on top and mixture #1 at the bottom resulted in model D and vice versa for model E.

b) Heterogeneous phantoms with inclusions: Inclusion phantoms with different characteristics were made into a single container. Three cylindrical molds with diameters of 10, 15, and 20 mm were glued to the bottom of the container. Each cylindrical mold was made of acrylonitrile butadiene styrene (ABS) and was fabricated by 3-D-printing (Dimension Elite, Stratasys Inc., Eden Prairie, MN, USA). Mixture #1 was poured into the container with ABS cylindrical molds in it, and the molds were removed after jellification. The resulting holes were filled with mixture #2.

2) Data Acquisition and Postprocessing: A Verasonics Vantage 256 scanner (Redmond, WA, USA) equipped with an ATL L7-4 probe (Philips, Bothell, WA, USA) driven at 5 MHz was used to perform US acquisitions. Coherent compounding was done with 21 angles ($-10°$ to $10°$), and 100 frames were acquired for each phantom. The f-k migration method was used for beamforming RF data [53]. To allow comparing results obtained with the proposed PF attenuation method with those of the SLD method using the same LASSO regularization approach, acquisitions with the same settings were made on a reference phantom (117GU-101 CIRS, Norfolk, VA, USA). For the subset of results with the inclusion phantoms, a median filter (MF) with a window size of 5×5 pixels was applied on PF attenuation images to compare with results using regularization.

3) Gold-Standard Attenuation Measurements: ACS ground-truth values (dB cm^{-1} MHz^{-1}) were estimated on pieces of the same phantoms made with mixtures #1 and #2, using a planar reflection method, with the same probe and system settings as for acquisitions on gel samples [36]. A cubic piece of each phantom was put onto a glass reflector in distilled water, and attenuation was estimated by measuring the amplitude difference of the US signal reflected by the glass plate, with and without the sample in the path.

B. In Vivo Liver Data Description

Four human liver US datasets were used to test the effectiveness of ACS methods. In vivo data included a healthy liver, a steatotic liver, a liver with a primary HCC, and another with metastatic cancer. Clinical protocols were approved by the institutional review board of the *Centre Hospitalier de l'Université de Montréal*. All recruited participants gave written informed consent.

1) Nonalcoholic Fatty Liver Disease (NAFLD): Nonalcoholic in vivo human liver datasets with different pathological conditions were investigated in two participants. The MRI proton density fat fraction (PDFF) was used to grade liver steatosis [54], [55]. The Achieva TX 3T MRI system (Philips Healthcare, Best, The Netherlands) was used, and the protocol consisted of using a two-channel body coil for transmission and a 16-channel surface array coil for signal reception with a 3-D chemical-shift encoded multiecho gradient-echo sequence using six echoes (mDixon Quant). The water/fat separation was performed in the complex-domain using a multifrequency spectral fat model and a T2$*$ correction. A low flip angle was used to avoid T1 bias. A liver biopsy was also available to assess the whole spectrum of the disease. The first participant had a histological steatosis grade of zero (S0) indicating the absence of steatosis. The second patient had a steatosis grade 2 (S2) indicating moderate steatosis.

2) Liver Cancers: Two in vivo human liver cancers were studied. The diagnosis was made using MRI as the reference standard. One patient had a circular 15-mm HCC mass, and the other one had one lesion corresponding to a colorectal liver metastasis (oval mass of 20×49 mm).

3) Data Acquisition and Postprocessing: The same Verasonics US system as for phantom experiments was used to collect 30 frames of data for each liver using a curvilinear array transducer (ATL C5-2, Philips) driven at 3.1 MHz. Coherent compounding was done with 21 angles ($-10°$ to $10°$) using the f-k RF data migration [53]. The same probe and system settings were used to acquire US data on a reference phantom for the SLD method.

C. Parameter Settings of ACS Algorithms

For phantom experiments, all computations were done in the Cartesian domain (x–z). To compare the performance of the phantom-free regularization approach, the SLD method was implemented according to our previous work [31], and the equations are provided in Appendixes. The power spectra of the proposed PF and SLD methods were averaged over 25 scan lines, each spanning ten pulse lengths on overlapping windows. For in vivo liver datasets, computations were done in the polar domain ($r - \theta$). To compare the performance of ACS methods, all parameters were set to the same values as for phantom experiments.

As an extra comparison for homogenous phantoms, the RFM was used with a CW with a size equal to 2.5×2.5 cm and within the range of frequency of 4–6 MHz in accordance with [42]. No attenuation maps were provided for this method because the size of the CW was much larger than for PF and SLD methods.

D. Data Analysis

To compare experimental results on phantoms, biases were calculated as the difference of mean values with the ground truth. Also, the normalized root mean square errors (NRMSEs) were computed as follows:

$$\text{NRMSE} = \frac{1}{\bar{x}} \sqrt{\frac{\sum_{i=1}^{N} (x_i - \hat{x}_i)^2}{N}} \tag{18}$$

where $\bar{x}$ represents the mean attenuation among N datasets, x_i is the ground-truth value at the i th position, and $\hat{x}_i$ represents the estimated value at the same position. For both biases and NRMSEs, standard deviations (SDs) were also calculated.

The contrast-to-noise ratio (CNR) for AC maps in the case of side-by-side, top-to-bottom, inclusion phantoms, and liver cancers was computed as

$$\text{CNR} = \frac{|\bar{x}_{m1} - \bar{x}_{m2}|}{\sqrt{\sigma_{m1}^2 + \sigma_{m2}^2}} \tag{19}$$

TABLE I

COMPARISON OF BIASES, NRMSES, AND CNRS FOR ATTENUATION MAPS OF PHANTOMS CORRESPONDING TO MODELS A–E OBTAINED WITH THE PROPOSED PF, SLD, AND RFM BEFORE AND AFTER REGULARIZATION (R)

		PF		PF-R		SLD		SLD -R		RFM	
Model		Medium #1	Medium #2	Medium #1	Medium #2	Medium #1	Medium #2	Medium #1	Medium #2	Medium #1	Medium #2
A	Bias (dB/cm/MHz)	-0.06 ± 0.03	-	0.04 ± 0.07	-	-0.09 ± 0.06	-	-0.06 ± 0.05	-	-0.15 ± 0.07	-
	NRMSE (%)	15.1 ± 2.1	-	8.9 ± 3.6	-	51.2 ± 5.1	-	19.2 ± 5.1	-	62.0 ± 10.6	-
B	Bias (dB/cm/MHz)	-	0.26 ± 0.12	-	-0.07 ± 0.02	-	-0.32 ± 0.11	-	-0.10 ± 0.08	-	-0.23 ± 0.18
	NRMSE (%)	-	13.5 ± 1.0	-	7.0 ± 1.6	-	42.6 ± 8.2	-	18.85 ± 6.1	-	34.9 ± 9.6
C	Bias (dB/cm/MHz)	0.09 ± 0.07	0.10 ± 0.06	0.05 ± 0.01	-0.01 ± 0.07	-0.07 ± 0.23	0.23 ± 0.23	-0.07 ± 0.18	-0.11± 0.12	-	-
	NRMSE (%)	35.1 ± 2	44.3 ± 1.2	11.3 ± 1.0	21.2 ± 5.0	45.6 ± 4.9	49.2 ± 6.3	19.2 ± 4.3	25.3 ± 8.1	-	-
	CNR	1.74 ± 0.07		3.54 ± 0.41		0.86 ± 0.04		1.75 ± 0.09		-	-
D	Bias (dB/cm/MHz)	0.06 ± 0.08	0.07 ± 0.03	0.04 ± 0.06	0.01 ± 0.05	-0.08 ± 0.31	0.18 ± 0.11	-0.06 ± 0.13	-0.14 ± 0.11	-	-
	NRMSE (%)	30.3 ± 3.2	38.4 ± 0.2	10.1 ± 3.2	17.4 ± 0.02	41.7 ± 5.2	45.2 ± 2.1	17.2 ± 3.4	20.3 ± 5.1	-	-
	CNR	1.72 ± 0.08		2.66 ± 0.31		0.70 ± 0.09		2.09 ± 0.14		-	-
E	Bias (dB/cm/MHz)	0.05 ± 0.09	0.09 ± 0.08	0.05 ± 0.02	0.08 ± 0.05	-0.13 ± 0.12	0.11 ± 0.13	-0.11 ± 0.07	-0.08 ± 0.13	-	-
	NRMSE (%)	30.3 ± 3.2	45.4 ± 7.2	9.3 ± 2.2	22.4 ± 8.6	43.9 ± 7.2	49.2 ± 6.3	27.3 ± 5.4	24.2 ± 7.1	-	-
	CNR	1.72 ± 0.12		3.41 ± 0.6		0.79 ± 0.13		2.12 ± 0.35		-	-

where $\bar{x}$ and σ are mean and SD of ACS values within the medium #1 ($m1$) and medium #2 ($m2$), corresponding to both tissues present or expected (i.e., either side-by-side or top-to-bottom media, gel surrounding or within the phantom inclusion, or liver parenchyma versus tumor, respectively).

A one-way analysis of variance (ANOVA) with repeated measures was performed on mean values of the two ACS methods evaluated on phantoms, with the presence or not of regularization as the cofactor. In the case where the Shapiro–Wilk normality test failed, the Friedman test was used as the nonparametric analog. In these tests, the sample size was 55, including ten homogeneous phantom acquisitions, three side-by-side phantom acquisitions, six top-to-bottom phantom acquisitions, and 36 inclusion phantom acquisitions. For Centre National de la Recherche Scientifique (CNRS), the sample size of the ANOVA test was 45 (homogenous phantoms were excluded). The Sigmaplot software (version 11.0.0, Systat, Palo Alto, CA, USA) was used to perform statistical analyses.

For in vivo NAFLD data, as there was no ground truth, the comparison of ACS methods with and without regularization was done by comparing mean values and coefficients of variation (CV = SD/mean) within the ROI. For in vivo cancer data, mean values and CNRs were used for comparison. The positions of lesion and background tissues were found by an expert radiologist based on MRI. CNRs for cancer data were computed based on one rectangle within the lesion and two rectangles within the liver parenchyma on top and bottom of the lesion (see Fig. 8). One can compute a single CNR value based on the whole rectangle. In order to compute the SD for this value, two other CNRs values were also computed based on two smaller rectangles within predefined rectangles. The SDs were computed based on these three CNR values.

IV. RESULTS

A. Experimental Phantoms

Local ACS maps obtained with both PF and SLD methods for models A–E are presented in Figs. 3 and 4. Maps without regularization are presented first and then compared with those obtained with regularization (indicated with -R). In the bottom row of Figs. 3 and 4, mean ACS values for different axial positions are compared with ground-truth (±SD) measurements obtained with the planar reflection method, which are 0.56 ± 0.07 dB cm^{-1} MHz^{-1} (for 4.5% graphite powder concentration, medium #1) and 1.15 ± 0.10 dB cm^{-1} MHz^{-1} (for 12% concentration, medium #2), respectively.

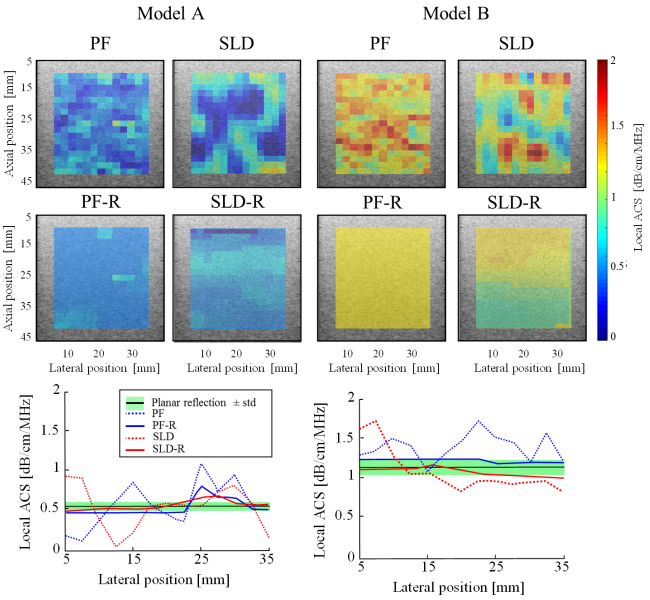

Fig. 3. Local attenuation maps obtained with PF and SLD methods for experimental phantoms with medium #1 (model A) and medium #2 (model B). The first and second rows show attenuation maps without and with regularization (R), respectively. The bottom row presents the comparison of mean ACS estimated with PF, PF-R, SLD, and SLD-R methods for the two models. Green regions in the graphs of the bottom row show means and SDs for ground-truth measurements with the planar reflection method.

Biases and NRMSE obtained by PF and SLD methods for phantom models A–E are presented in Table I. The bias in dB cm^{-1} MHz^{-1} for the first homogeneous phantom (model A)

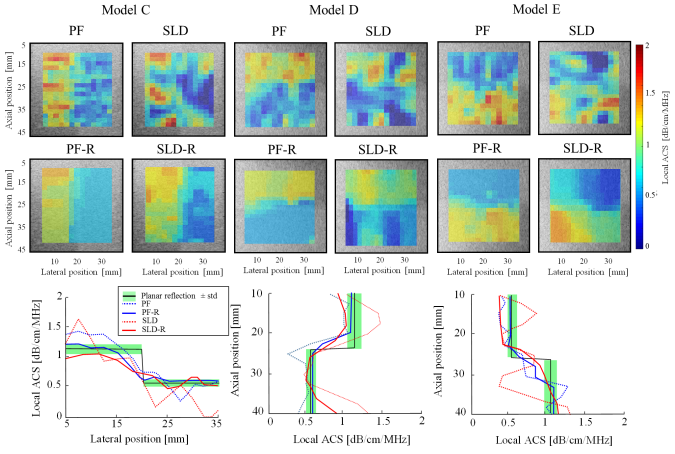

Fig. 4. Local attenuation maps obtained with PF and SLD methods for experimental phantoms with side-by-side medium #1 on the right and #2 on the left (model C), top-to-bottom medium #1 on the bottom and #2 on the top (model D), and vice versa (model E). The first and second rows show attenuation maps without and with regularization (R), respectively. The bottom row presents the comparison of mean ACS estimated with PF, PF-R, SLD, and SLD-R methods for the three models. Green regions in graphs of the bottom row show means and SDs for ground-truth measurements with the planar reflection method.

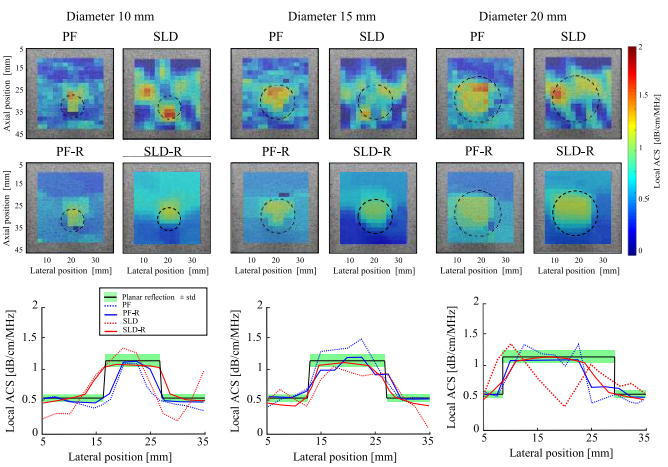

Fig. 5. Local attenuation maps for experimental phantoms with inclusion diameters of 10, 15, and 20 mm with PF and SLD methods. The first and second rows show attenuation maps without and with regularization (R), respectively. The bottom row presents the comparison of mean ACS estimated with PF, PF-R, SLD, and SLD-R methods for the three inclusion sizes. Green regions in graphs of the bottom row show means and SDs for ground-truth measurements with the planar reflection method.

with three acquisitions was close in absolute value for PF, phantom-free regularized (PF-R), SLD, SLD-R, and RFM at -0.06 ± 0.03, 0.04 ± 0.07, -0.09 ± 0.06, -0.06 ± 0.05, and -0.15 ± 0.07, respectively. The same trends were emphasized for the second more attenuating homogeneous phantom (model B). Biases for the PF, PF-R, SLD, SLD-R, and RFM were 0.26 ± 0.12, -0.07 ± 0.02, -0.32 ± 0.11, -0.10 ± 0.05, and -0.23 ± 0.18, respectively. As indicated in Table I, trends in favor of the PF-R method were confirmed when analyzing NRMSEs. Results show that the PF-R method yielded lower NRMSEs compared with SLD-R and RFM, and those differences were emphasized without regularization for SLD. The largest mean of biases and NRMSEs were obtained with the SLD method that was used in this study for comparison.

With side-by-side and top-to-bottom media (models C–E), each based on three acquisitions, biases and NRMSEs were smaller, similar, or higher than for homogeneous phantoms (see Table I). Biases and NRMSEs obtained with the PF-R method were generally less for both media. The PF-R had the highest CNR compared to the other methods. Furthermore, according to the bottom row of Fig. 4, the PF with regularization made a distinct differentiation at the boundary of both media, whereas the SLD method with regularization had a smoother transition.

B. Phantoms With Inclusions

Local ACS maps given by PF and SLD methods, without and with regularization, are presented graphically in the first and second rows of Fig. 5, respectively. Inclusions are visually emphasized with black dashed line circles on attenuation maps. The PF method has smoother maps than the SLD method, and inclusions are visually more detectable. After regularization, inclusions are identifiable with both PF-R and SLD-R methods. According to Table II, in the case of smaller inclusions of 10 and 15 mm diameters, the biases within inclusions were larger, and the NRMSEs were less with the PF method compared to SLD. On the other hand, the PF had a better estimation of ACS outside inclusions (lower biases and NRMSEs), i.e., within homogeneous regions of phantoms. For the largest inclusion of 20 mm, the bias of the PF method is higher than for the SLD method within the inclusion. However, it is the other way around in the surrounding tissue. The average of absolute bias values of both regions of phantoms with the PF and PF-R methods is generally less than with the SLD and SLD-R methods. The same trend was observed with NRMSE values. After regularization, the bias and NRMSE in all regions are decreased; PF-R with regularization had the lowest mean biases and NRMSEs over all inclusion phantoms. It shows that the regularization increased CNR values for both PF and SLD methods. Higher CNRs were obtained for bigger inclusions with the PF-R method. PF-R and SLD-R had similar CNRs in the case of the 10-mm-diameter inclusion.

According to the bottom row of Fig. 5, the SLD-R method has smoother transitions between the surrounding tissue and the inclusion, thus reducing the lesion detectability but improving the size detection compared with the proposed method. Differences tend to disappear for the larger inclusion of 20 mm. In general, ACS results with the proposed regularized method (PF-R) are closer to ground-truth values.

Overall, the means of absolute biases from the 55 experimental datasets, including homogeneous, side-by-side, top-to-bottom, and inclusion phantoms, were 0.17 ± 0.06, 0.14 ± 0.05, 0.23 ± 0.07, and 0.20 ± 0.07 dB cm^{-1} MHz^{-1} ($p < 0.001$) for PF, PF-R, SLD, and SLD-R methods, respectively. Mean NRMSEs of PF, PF-R, SLD, and SLD-R methods from all 55 datasets were 41.7 ± 10.2, 32.9 ± 12.9, 76.0 ± 27.5, and 46.1 ± 19.4 % ($p < 0.001$), respectively. Also, the means of CNRs from 45 experimental datasets, including side-by-side, top-to-bottom, and inclusion phantoms, were 1.18 ± 0.49, 1.69 ± 0.95, 0.51 ± 0.21, and 1.37 ± 0.62 ($p < 0.001$)

TABLE II

COMPARISON OF BIASES, NRMSES, AND CNRS FOR ATTENUATION MAPS OF PHANTOMS WITH INCLUSION DIAMETERS OF 10, 15, AND 20 MM OBTAINED WITH THE PROPOSED PF AND SLD METHODS WITHOUT AND WITH REGULARIZATION (R)

		PF		PF-R		SLD		SLD -R	
D		Inclusion	Tissue	Inclusion	Tissue	Inclusion	Tissue	Inclusion	Tissue
10 mm	Bias (dB/cm/MHz)	-0.20 ± 0.06	-0.10 ±0.04	-0.16 ± 0.07	-0.04 ± 0.05	-0.07 ± 0.18	-0.25 ± 0.12	-0.08 ± 0.21	0.11 ± 0.09
	NRMSE (%)	33.1 ± 6.7	26.2 ±5.1	22.0 ± 6.2	25.4 ± 8.1	53.1 ± 9.1	63.2 ± 5.3	42.7 ± 5.6	32.7 ± 9.4
	CNR	0.86 ± 0.24		1.26 ± 0.38		0.59 ± 0.17		0.91 ± 0.13	
15 mm	Bias (dB/cm/MHz)	-0.26 ± 0.08	-0.13 ± 0.04	-0.14 ± 0.12	-0.05 ± 0.09	-0.17 ± 0.15	0.26 ± 0.21	-0.08 ± 0.21	0.19 ± 0.17
	NRMSE (%)	31.2 ± 6.3	36.3 ± 16.1	15.1 ± 5.0	21.2 ± 7.1	47.2 ± 9.3	90.3 ± 25.2	32.18 ± 6.4	59.7 ± 15.1
	CNR	0.87 ± 0.41		1.05 ± 0.50		0.37 ± 0.24		0.92 ± 0.47	
20 mm	Bias (dB/cm/MHz)	-0.11 ± 0.03	-0.12 ± 0.01	-0.03 ± 0.1	-0.01 ± 0.07	-0.07 ± 0.23	0.23 ± 0.23	-0.09 ± 0.14	0.12 ± 0.14
	NRMSE (%)	25.2 ± 2.2	24.1 ± 1.1	11.7 ± 0.03	16.2 ± 1	40.3 ± 8.2	106.0 ± 29.2	13.1 ± 7.5	82.5 ± 41.7
	CNR	1.40 ± 0.46		1.63 ± 0.63		0.38 ± 0.23		1.37 ± 0.24	

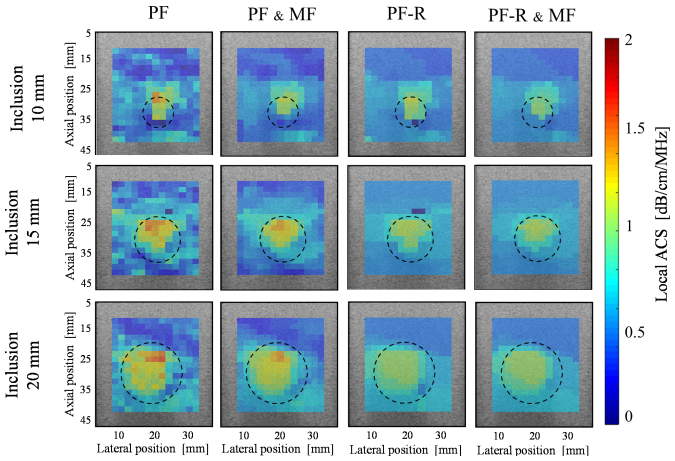

Fig. 6. Local attenuation maps for experimental phantoms with inclusions of 10, 15, and 20 mm using the PF, the same method after applying an MF (PF and MF), the PF method with regularization (PF-R), and results with PF-R and median filtering (PF-R and MF).

TABLE III

COMPARISON OF BIASES, NRMSES, AND CNRS FOR ATTENUATION MAPS OF PHANTOMS WITH INCLUSION DIAMETERS OF 10, 15, AND 20 MM OBTAINED AFTER APPLYING AN MF ON RESULTS OF THE PHANTOM-FREE METHOD (PF) OR PHANTOM-FREE METHOD WITH REGULARIZATION (PF-R)

		PF with median filter		PF–R with median filter	
D		Inclusion	Tissue	Inclusion	Tissue
10 mm	Bias (dB/cm/MHz)	-0.30 ± 0.05	-0.06 ± 0.04	-0.21 ± 0.06	-0.08 ± 0.05
	NRMSE (%)	29.0 ± 6.5	25.7 ± 4.2	22.0 ± 2.1	25.4 ± 6.1
	CNR	0.87 ± 0.21		1.29 ± 0.35	
15 mm	Bias (dB/cm/MHz)	-0.23 ± 0.08	-0.10 ± 0.05	-0.15 ± 0.06	-0.06 ± 0.06
	NRMSE (%)	23.2 ± 7.5	34.2 ± 7.3	14.1 ± 5.02	21.2 ± 0.04
	CNR	0.92 ± 0.45		1.15 ± 0.47	
20 mm	Bias (dB/cm/MHz)	-0.06 ± 0.2	-0.09 ± 0.09	-0.04 ± 0.07	-0.01 ± 0.04
	NRMSE (%)	17.0 ± 2.2	21.7 ± 1.1	10.2 ± 3.4	14.2 ± 6.01
	CNR	1.44 ± 0.44		1.69 ± 0.59	

with PF, PF-R, SLD, and SLD-R methods, respectively. This comparison shows that the PF method with regularization had the lowest biases and NRMSEs, and highest CNRs.

The PF and PF-R methods were also investigated with an MF; the biases and NRMSEs are provided in Table III. Results with median filtering of ACS maps are given in Fig. 6. According to Table III, the NRMSE for the PF method with median filtering in both regions of phantoms are smaller in comparison with the PF method (based on Table II), and absolute values of biases are also smaller, except in the case of the smallest inclusion (diameter of 10 mm). Moreover, the PF with regularization has smaller biases and NRMSEs, and also larger CNRs, compared with the median filtered PF method. With median filtering on PF-R results, absolute values of biases and CNRs are larger compared with the proposed PF-R method, but NRMSEs are smaller.

C. In Vivo Human Livers

In this section, as for phantom experiments, the results of PF and SLD methods are compared based on mean values and CVs within tumors and surrounding tissues. Also, CNRs are compared for attenuation maps obtained in the case of liver cancers.

1) Nonalcoholic Steatohepatitis: The left columns of Fig. 7(a) and (b) display the B-mode image and the ROI under investigation (red box) for livers with MRI fat fractions of 0.61% and 15.01%, respectively. For the healthy liver, means ± SDs in dB cm^{-1} MHz^{-1} obtained for PF and SLD methods are 0.45 ± 0.28 and 0.51 ± 0.47 without regularization, and 0.47 ± 0.20 and 0.67 ± 0.11 with PF-R and SLD-R, respectively. The smallest variability was obtained with the SLD-R method (CV of 16.4%). Similarly, local attenuation maps of the steatotic grade 2 liver provided ACS values for PF and SLD methods of 0.92 ± 0.19 and 1.14 ± 0.41 dB cm^{-1} MHz^{-1}, and after regularization, these values are 0.91 ± 0.08 and 1.06 ± 0.15 for PF-R and SLD-R, respectively. The PF-R method resulted in the smallest CV (8.8%), but differences in mean values are small.

2) Liver Cancers: Local attenuation maps without regularization estimated by PF and SLD methods for the human liver with HCC cancer are shown in the top row of Fig. 8(a). The detection and diagnosis of the lesion based on MRI were visually registered on US images. Yellow boxes on B-mode

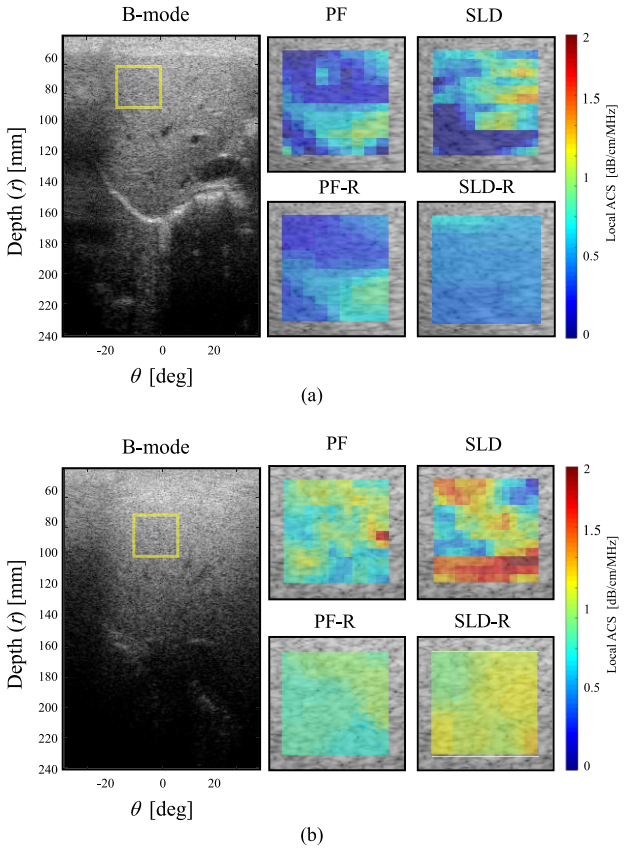

Fig. 7. ACS results for two in vivo human NAFLD datasets with MRI-determined PDFFs of 0.6% (corresponding to a histological grade S0) [(a) woman of 25 years old] and 15.0% (corresponding to a histological grade S2) [(b) woman of 52 years old], respectively. For each participant, the B-mode image and the ROI (yellow box) under investigation are presented, along with local attenuation maps within the ROI for PF and SLD methods (without and with regularization in the first and second rows, respectively).

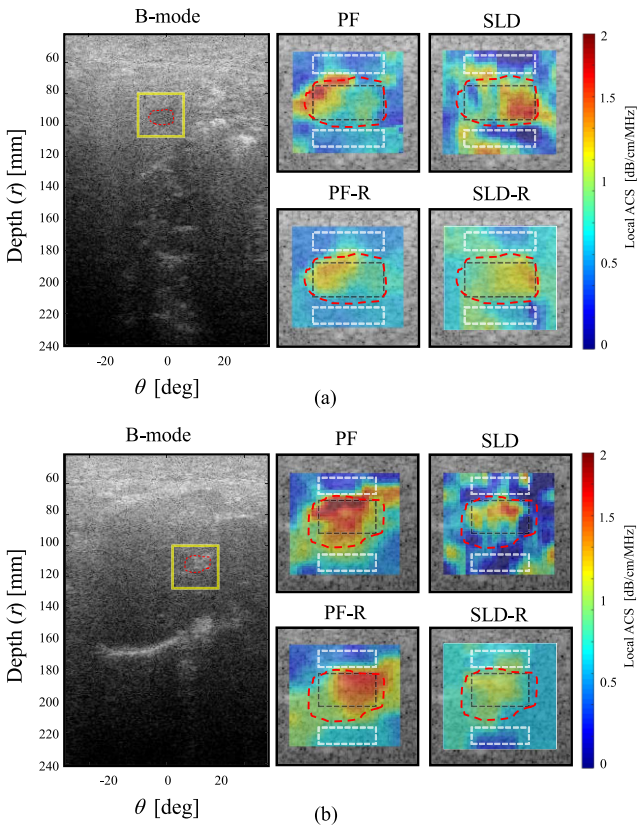

Fig. 8. Results for two in vivo human liver datasets with cancer: (a) liver HCC in the right lobe of a 55-year-old man and (b) colorectal liver metastasis in the left lobe of a 67-year-old woman. For each participant, the B-mode image is presented on the left with the identified ROI (yellow box) including the lesion. Right: local attenuation maps with PF and SLD methods without (top row) and with regularization (bottom row). The lesion positions are indicated with red dashed lines. The lesion and parenchyma tissue regions used for computing CNRs are indicated with black and white dashed-line rectangles, respectively.

images show the position of the ROI within the liver, which includes the lesion.

For CNR computations in Fig. 8, the position of the lesion and liver parenchyma on attenuation maps is displayed with black and white dashed-line rectangles, respectively. Means ± SDs in dB cm^{-1} MHz^{-1} and CNRs obtained for PF, PF-R, SLD, and SLD-R methods are provided in Table IV.

The lesion could be deduced from the ACS map produced by the PF method (a localized spot with high attenuation), but, in the case of the SLD method, several scattered areas with varying attenuations could be suspected as being a lesion. After regularization [see the bottom row of Fig. 8(a)], the lesion is visible on the PF map as a homogeneous area with the highest attenuation, but detectability on the regularized SLD map is less apparent. This could be also deduced from computed CNRs.

Both PF-R and SLD-R methods underestimated the size of the tumor compared with the B-mode counterpart. Maximum ACS values within the ROI containing the HCC lesion are 1.41 and 1.37 dB cm^{-1} MHz^{-1} for PF-R and SLD-R methods, respectively. The position of the maximum AC within the map did not coincide between methods.

Fig. 8(b) shows the second in vivo human liver dataset corresponding to metastatic liver cancer. Maps produced by the PF method whether regularization was used or not allow to clearly detect a lesion with high attenuation in the middle of the ROI, whereas detectability is more difficult on SLD maps. Maximum ACS values within the ROI with PF-R and SLD-R methods are 1.74 and 1.29 dB cm^{-1} MHz^{-1}, respectively. The PF-R method had the highest CNR compared to other methods.

V. Discussion

In this work, we demonstrated the theoretical basis for estimating local ACS without the need for a calibration phantom in the context of heterogeneous media, thus extending the work of Gong et al. [42], which was considering homogeneous structures. We also integrated the proposed PF method into a theoretical framework yielding regularized local ACS maps.

A method such as the SLD can be quite cumbersome for clinical trials because a phantom acquisition is necessary after the clinical US exam using the same probe and system settings. As mentioned, the proposed method was inspired by the RFM of Gong et al. [42], with the following novelties: a linear interpolation of the power spectrum in the log scale was used, the underlying hypothesis on the compression wave US probe diffraction factor was relaxed, a generalization

TABLE IV

COMPARISON OF MEANS AND CNRS FOR ATTENUATION MAPS OF TWO IN VIVO HUMAN LIVER DATASETS WITH CANCER. (A) LIVER HCC IN THE RIGHT LOBE OF A 55-YEAR-OLD MAN. (B) COLORECTAL LIVER METASTASIS IN THE LEFT LOBE OF A 67-YEAR-OLD WOMAN. MEANS AND CNRS ARE COMPUTED BASED ON RECTANGLE AREAS WITHIN THE LESION AND PARENCHYMA TISSUES

		PF		PF-R		SLD		SLD -R	
Liver Cancer		Lesion	Tissue	Lesion	Tissue	Lesion	Tissue	Lesion	Tissue
(a)	Mean (dB/cm/MHz)	0.95 ± 0.33	0.59 ± 0.19	1.01 ± 0.21	0.57 ± 0.10	1.12 ± 0.34	0.48 ± 0.39	1.08 ± 0.17	1.13± 0.24
	CNR	1.73 ± 0.76		2.31 ± 0.37		1.72 ± 0.58		2.02 ± 0.31	
(b)	Mean (dB/cm/MHz)	1.53 ± 0.23	0.67 ± 0.42	1.40 ± 0.26	0.56 ± 0.19	0.84 ± 0.48	0.47 ± 0.34	0.91 ± 0.22	0.72 ± 0.13
	CNR	2.34 ± 0.92		3.41 ± 1.14		0.95 ± 0.43		1.73 ± 0.82	

to heterogeneous local ACS was made, and an adaptive restriction on usable frequencies was implemented to consider a more reliable range than the usual −20-dB frequency range. Moreover, the framework of the regularization scheme proposed in our preliminary reports [31], [43] was better documented and also implemented in the framework of the SLD method. We could demonstrate equivalent or even smaller biases and NRMSEs than the classical SLD method on the in vitro dataset and equivalent or larger CNRs on the in vivo liver data. The addition of regularization to both proposed PF and classical SLD methods further allowed the appreciation of the performance of the phantom-free algorithm. Furthermore, applying an MF could also further reduce image variability, but it showed limitations in the case of small inclusion phantoms as filtering blurred boundaries. The overall procedure for constructing local ACS maps in this work is schematized in Fig. 9.

ACS estimates on both homogeneous and heterogeneous tissues represented a specific challenge, rarely addressed in the scientific literature [30]. The implementation of strategies listed in Fig. 2 allowed for obtaining promising phantom and proof-of-concept clinical results. Results based on the PF-R method on homogeneous, side-by-side, and top-to-bottom phantoms indicated that the proposed method could estimate ACS close to ground-truth values, and in all cases, NRMSEs decreased with regularization, which allowed differentiating visually the two media. CNRs also increased with regularization. The comparison of PF with the SLD algorithm showed that the proposed method had a better prediction at the border between the two media. Producing phantoms with top-to-bottom designs was of particular interest as it could mimic the more attenuating superficial thick layer of fat in patients with obesity (model D) or the accumulation of low-attenuating fluid in the liver of patients with ascites (model E).

The performance of the proposed method for detecting lesions in experimental phantoms with diameters varying from 10 to 20 mm was also investigated. Results showed that the proposed method could detect all lesions. Regularization increased the CNRs by reducing variances in both the inclusion and its surrounding. Since the CNR depends on mean values and variances within the inclusion and surrounding tissues, we do not expect a trend of CNR with the inclusion's size. This can be observed in the values reported in Table II.

We also examined the influence of an MF on attenuation maps of the PF method without and with regularization. The regularization had lower biases and NRMSEs compared with simple median filtering. Applying filters on regularized attenuation maps could further improve results due to the smoothening effect on ACS maps and increase in CNRs, which is a common task in image processing [56]. Notice that, in the case of small inclusions, an MF can increase the bias and blur boundaries, which are not desirable.

The proposed method was also tested on two in vivo human NAFLD data. Results obtained were in the range of values reported in the literature [57], [58], [59]. The proposed method provided smaller variability than SLD for each clinical case. Coefficients of variation showed reduction after regularization. Differences between both datasets in terms of local ACS were observed, and the liver with a steatosis grade 2 showed a higher attenuation. This is in line with recent clinical reports using clinical systems where ACS could correlate with the MRI-PDFF or biopsy staging. According to recent works, attenuation had increasing trends with higher steatosis grades [60], [61]. Therefore, this method may be utilized as a biomarker for the diagnosis of liver steatosis.

Finally, the proposed method was evaluated in the case of two in vivo human livers with cancer. Lesions were detectable with both PF and SLD methods with regularization. The higher AC on liver images of patients with secondary cancer than primary HCC (as seen in Fig. 8) was also recently observed in therapeutic US applications; in this report, however, no attenuation images were provided [62]. Notice that, in Fig. 8, shadowing below the lesion's areas is not visible despite the high local ACS values within these two lesions reported in Table IV. We believe that this might be due to the small size of the lesions and also to multiangle plane wave compounding (one may expect posterior shadowing for a highly attenuating lesion with conventional clinical scanner's imaging) [63].

To the best of our knowledge, ACS imaging has not yet been used for detecting and characterizing liver cancer. In addition to the fact that the proposed method does not use a reference phantom for ACS estimation, our proof of concept on liver cancer datasets is opening the opportunity to use this new imaging contrast for the diagnosis of liver cancer.

One of the limitations of this work is that only one computation window size was considered to reconstruct attenuation maps for both PF and SLD methods. There is always a tradeoff between resolution and accuracy of estimation. Hence, additional studies are needed to find the optimum CW's size for a specific clinical application without affecting too much the resolution of attenuation maps. There are also other types of regularization that may improve the reconstruction

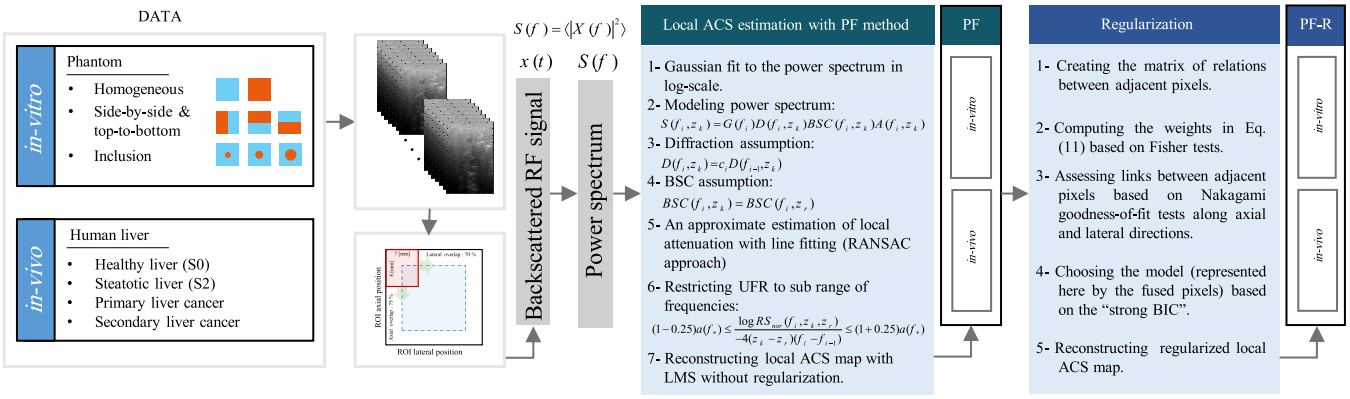

Fig. 9. Summary of the proposed procedure for constructing local ACS maps with PF and PF-R methods on in vitro and in vivo data.

of parametric maps [34], [35]. Moreover, the size of CWs could affect the Nakagami model, especially in the case of long CWs. Also, overlapping of CWs could prevent the assumption of independent identically distributed residual noise to hold although it is common to make this assumption in the case of overlapping windows [34], [64]; this potential issue should be investigated in future studies. Furthermore, although the power spectrum of backscattered RF signals is assumed approximately Gaussian in many medical US applications [65], there are nonetheless cases where this assumption would not hold. However, other models could be adopted to fit power spectra [66], an avenue that could be investigated in future studies.

Finally, based on obtained in vivo results, the proposed method may certainly provide additional information to clinicians for the diagnosis of liver steatosis and detection of suspected cancerous lesions visible on the B-mode US. The ultimate goal would be to improve the detection of HCC in the early stages when it is not visible on B-mode images.

VI. Conclusion

A method, inspired by the work of Gong et al. [42], was presented for estimating local ACS based on the frequency and depth normalization without the need for a calibration phantom. The proposed method was tested on homogeneous, side-by-side, top-to-bottom, and heterogeneous phantoms with inclusions. Also, the performance of the proposed method was assessed in the case of four in vivo human livers consisting of one normal case, one stage 2 steatotic liver, one liver with a primary HCC, and one with a secondary metastatic cancer. The proposed method uses a linear interpolation of the power spectrum in the log scale, the relaxation of the underlying hypothesis on the wave diffraction factor, and an adaptive restriction of frequencies to a more reliable range than the usual −20-dB UFR. Moreover, a generalization to nonhomogeneous local ACS has been proposed. Furthermore, a regularization procedure, which was formulated as a generalized LASSO, and a variant of the BIC were applied to estimate the Lagrangian multiplier on the LASSO constraint. It was shown that applying regularization overall improved local ACS maps. In future works, further validation on larger in vivo datasets should be conducted, and the performance of the proposed method with different beamforming approaches should also be investigated.

Appendix A

The data fidelity term and the constraint matrix of Section II-C are explained in the case of the SLD model in this appendix. Let us recall that, in the SLD method, one considers two nonoverlapping windows within the CW at proximal and distal depths z_p and z_d, respectively. Attenuation factors at depths z_p and z_d, for either samples or the reference phantom, are of the form

$$A(f, z_p) = \exp\left(-4\alpha_{\text{total}} z_p f\right) \tag{A-1a}$$

$$A(f, z_d) = \exp\left(-4\left(\alpha_{\text{total}} z_p + \alpha_{\text{local}} \Delta z\right) f\right) \tag{A-1b}$$

where α_{total} and α_{local} denote the total and local ACSs, respectively, and $\Delta z = z_d - z_p$. Furthermore, one assumes that backscatter coefficients at two depths within an ROI are proportional, which, under the Gaussian scattering model, means that the effective scatterers' radius remains fixed within the ROI, but the acoustic concentration might vary [15]. One then computes the relation [15]

$$\log \frac{\text{PS}_S(f, z_p)}{\text{PS}_S(f, z_d)} - \log \frac{\text{PS}_{\text{ref}}(f, z_p)}{\text{PS}_{\text{ref}}(f, z_d)} = 4\Delta\alpha_{\text{local}} \Delta z f + \text{const} \tag{A-2}$$

where $\Delta\alpha_{\text{local}}$ is the difference in local ACS between samples and the reference phantom. Thus, the observed spectral data on the left-hand side of (A-2) are

$$y_r = \left(\log \frac{\text{PS}_S(f, z_p)}{\text{PS}_S(f, z_d)} - \log \frac{\text{PS}_{\text{ref}}(f, z_p)}{\text{PS}_{\text{ref}}(f, z_d)} \right)_{i=1}^{N_{\text{Freq}}}. \tag{A-3a}$$

The predictors' matrix and regression coefficients are finally of the form

$$X_r = \left(4 f_i \Delta z_r \;\; 1\right)_{i=1}^{N_{\text{Freq}}} \tag{A-3b}$$

$$\beta_r = \left(\beta_{r,1} \;\; \beta_{r,2}\right)^T \tag{A-3c}$$

$$\beta_{r,1} = \Delta\alpha_{r,\text{local}}. \tag{A-3d}$$

The weights w_r in (11) were kept to 1.

Since, in the case of the SLD model, the vector of regression coefficients has dimension d greater than 1 ($d = 2$), its components might be of different orders of magnitude. Thus, the ℓ_1-norm regularization term in (13a) was replaced with

$$\text{reg}_1(\beta, \lambda) = \lambda \sum_{r=1}^{N_{\text{CW}}} \sum_{m=1}^{d} a_m \sum_{s \in N(r)} \left|\beta_{r,m} - \beta_{s,m}\right| \tag{A-4a}$$

TABLE V
COMPARISON OF RFM AND PF METHODS ON TWO HOMOGENEOUS PHANTOMS AND INVESTIGATION OF THE EFFECT OF EACH MODIFICATION

	Method	Modifications					Bias Medium #1 (dB cm^{-1} MHz^{-1})	R	Bias Medium #2 (dB cm^{-1} MHz^{-1})	R
		A	B	C	D	E				
1	RFM	2.5 cm	4-6 MHz				-0.15		-0.23	
2		✓	4-6 MHz				0.97	0.81	-0.40	-0.33
3		✓	✓				0.38		-0.20	
4		✓	✓	✓			-0.37		-0.54	
5		✓	✓	✓	✓		0.12		0.48	
6	Proposed	✓	✓	✓	✓	✓	0.06	0.04	0.26	-0.07

A: Computing window (size = 0.7 cm), B: usable frequency range (UFR), C: log-scale Gaussian fit, D: adaptive frequency sub-range, E: modified RANSAC approach, and R: regularization

where a_m, $m = 1, 2$, are the weights of the regression coefficients. The LMSE problem was first solved without regularization, and then, the weights were set to

$$a_1 = \frac{\frac{1}{\|(\beta_{r,1}+\alpha_{\text{ref}})\|_1}}{\frac{1}{\|(\beta_{r,1}+\alpha_{\text{ref}})\|_1} + \frac{1}{\|(\beta_{r,2})\|_1}} \tag{A-4b}$$

$$a_2 = \frac{\frac{1}{\|(\beta_{r,2})\|_1}}{\frac{1}{\|(\beta_{r,1}+\alpha_{\text{ref}})\|_1} + \frac{1}{\|(\beta_{r,2})\|_1}} \tag{A-4c}$$

where $(\beta_{r,1}, \beta_{r,2})$ denotes the initial LMSE solution. In particular, sum up to 1, the terms in (A-4a) are now of comparable order of magnitude.

APPENDIX B

In this section, the comparison between RFM and the proposed method is provided by considering each modification brought to the RFM (see the impact of each step implementation in Table V). As mentioned in [42] and [67], the RFM has been used only in the case of a homogeneous medium, and a square computation window of about 2.5 cm side length was considered.

The most important innovations in our work can be summarized into the following features: 1) the smaller CW's size; 2) the UFR; 3) the log-scale Gaussian fit; 4) the adaptive frequency subrange of the UFR; and 5) the modified RANSAC line fitting.

In the initial state of the method [42], the CW was a square with sides of 2.5 cm, and the frequency range was fixed between 4 and 6 MHz. With this configuration in Table V, the RFM had a good estimation of attenuation on the first phantom (bias of -0.15) but a larger underestimation on the second phantom (bias of -0.23).

In the second state (condition A), the CW size was decreased (as in our implementation of PF and SLD methods). It can be observed that the RFM failed with such a small window's size, and even the estimated attenuation for medium #2 was less than for medium #1, which should be the opposite trend. In the third state (condition A + B), by changing the frequency range used in RFM (4–6 MHz) to the UFR, the biases for both phantoms decreased, and the attenuation estimated for medium #2 was slightly higher than medium #1, but the biases were still large. In the fourth state (conditions A + B + C), a log scale Gaussian fit was applied to the previous improvements. It can be observed that, although the bias for medium #2 was increased, the difference in estimated attenuation for the two media was nevertheless larger. In the fifth state (conditions A + B + C + D), by considering the adaptive frequency range within the URF, the biases were much smaller in both cases, and the trend of estimated attenuations was correct in both media. For the final improvement considered with the proposed method (the sixth state, conditions A + B + C + D + E), by adding the proposed modified RANSAC line-fitting criterion, the biases were much reduced.

We also considered comparing the RFM and the proposed method with regularization. However, it was not applicable with the large CW size recommended by Gong et al. [42], [67] due to a resulting lack of memory, as this implies several subwindows. Nonetheless, regularization was performed on the RFM with small CWs (state 2). The resulting absolute biases were larger than those obtained with the proposed method either with or without regularization.

ACKNOWLEDGMENT

The authors acknowledge the contribution of Marie-Hélène Roy Cardinal (B.Eng. and Ph.D.) and Boris Chayer (B.Eng. and M.Eng.) for helpful discussions and suggestions on statistics and phantom fabrication, respectively.

REFERENCES

[1] H. B. El–Serag and K. L. Rudolph, "Hepatocellular carcinoma: Epidemiology and molecular carcinogenesis," *Gastroenterology*, vol. 132, no. 7, pp. 2557–2576, Jun. 2007.
[2] J. M. Llovet et al., "Hepatocellular carcinoma," *Nature Rev. Disease Primers*, vol. 7, no. 1, p. 6 Jan. 2021.
[3] A. Villanueva, "Hepatocellular carcinoma," *New England J. Med.*, vol. 380, no. 15, pp. 1450–1462, Apr. 2019.
[4] J. D. Yang, P. Hainaut, G. J. Gores, A. Amadou, A. Plymoth, and L. R. Roberts, "A global view of hepatocellular carcinoma: Trends, risk, prevention and management," *Nature Rev. Gastroenterol. Hepatol.*, vol. 16, no. 10, pp. 589–604, Oct. 2019.
[5] W. Wang and C. Wei, "Advances in the early diagnosis of hepatocellular carcinoma," *Genes Diseases*, vol. 7, no. 3, pp. 308–319, Sep. 2020.
[6] S. M. Bierig and A. Jones, "Accuracy and cost comparison of ultrasound versus alternative imaging modalities, including CT, MR, PET, and angiography," *J. Diagnostic Med. Sonography*, vol. 25, no. 3, pp. 138–144, May 2009.
[7] A. Singal et al., "Meta-analysis: Surveillance with ultrasound for early-stage hepatocellular carcinoma in patients with cirrhosis," *Alimentary Pharmacol. Therapeutics*, vol. 30, no. 1, pp. 37–47, Jul. 2009.
[8] A. Colli et al., "Accuracy of ultrasonography, spiral CT, magnetic resonance, and alpha-fetoprotein in diagnosing hepatocellular carcinoma: A systematic review," *Official J. Amer. College Gastroenterol.*, vol. 101, no. 3, pp. 513–523, Mar. 2006.
[9] R. Chou et al., "Imaging techniques for the diagnosis of hepatocellular carcinoma: A systematic review and meta-analysis," *Ann. Internal Med.*, vol. 162, no. 10, pp. 697–711, May 2015.
[10] P. Del Poggio et al., "Factors that affect efficacy of ultrasound surveillance for early stage hepatocellular carcinoma in patients with cirrhosis," *Clin. Gastroenterol. Hepatol.*, vol. 12, no. 11, pp. 1927–1933, Nov. 2014.
[11] R. N. Uppot, D. V. Sahani, P. F. Hahn, M. K. Kalra, S. S. Saini, and P. R. Mueller, "Effect of obesity on image quality: Fifteen-year longitudinal study for evaluation of dictated radiology reports," *Radiology*, vol. 240, no. 2, pp. 435–439, Aug. 2006.

[12] G. Cloutier, F. Destrempes, F. Yu, and A. Tang, "Quantitative ultrasound imaging of soft biological tissues: A primer for radiologists and medical physicists," *Insights Imag.*, vol. 12, no. 1, p. 127, Sep. 2021.

[13] E. A. Omari, T. Varghese, E. L. Madsen, and G. Frank, "Evaluation of the impact of backscatter intensity variations on ultrasound attenuation estimation," *Med. Phys.*, vol. 40, no. 8, Jul. 2013, Art. no. 082904.

[14] E. Omari, H. Lee, and T. Varghese, "Theoretical and phantom based investigation of the impact of sound speed and backscatter variations on attenuation slope estimation," *Ultrasonics*, vol. 51, no. 6, pp. 758–767, Aug. 2011.

[15] Y. Labyed and T. A. Bigelow, "A theoretical comparison of attenuation measurement techniques from backscattered ultrasound echoes," *J. Acoust. Soc. Amer.*, vol. 129, no. 4, pp. 2316–2324, 2011.

[16] K. J. Taylor et al., "Quantitative U.S. attenuation in normal liver and in patients with diffuse liver disease: Importance of fat," *Radiology*, vol. 160, no. 1, pp. 65–71, Jul. 1986.

[17] M. Sasso et al., "Controlled attenuation parameter (CAP): A novel VCTE guided ultrasonic attenuation measurement for the evaluation of hepatic steatosis: Preliminary study and validation in a cohort of patients with chronic liver disease from various causes," *Ultrasound Med. Biol.*, vol. 36, no. 11, pp. 1825–1835, Nov. 2010.

[18] Y. N. Zhang et al., "Liver fat imaging—A clinical overview of ultrasound, CT, and MR imaging," *Brit. J. Radiol.*, vol. 91, no. 1089, Sep. 2018, Art. no. 20170959.

[19] E. Roldan-Valadez, R. Favila, M. Martínez-López, M. Uribe, and N. Méndez-Sánchez, "Imaging techniques for assessing hepatic fat content in nonalcoholic fatty liver disease," *Ann. Hepatology*, vol. 7, no. 3, pp. 212–220, Jul. 2008.

[20] C. D. Byrne and G. Targher, "NAFLD: A multisystem disease," *J. Hepatol.*, vol. 62, no. 1, pp. 47–64, Apr. 2015.

[21] S. K. Venkatesh, V. Chandan, and L. R. Roberts, "Liver masses: A clinical, radiologic, and pathologic perspective," *Clin. Gastroenterol. Hepatol.*, vol. 12, no. 9, pp. 1414–1429, Sep. 2014.

[22] P. H. Lima et al., "Cost-utility analysis of imaging for surveillance and diagnosis of hepatocellular carcinoma," *Amer. J. Roentgenol.*, vol. 213, no. 1, pp. 17–25, Jun. 2019.

[23] T. A. Bigelow and Y. Labyed, "Attenuation compensation and estimation," in *Quantitative Ultrasound in Soft Tissues*, J. Mamou and M. L. Oelze, Eds. Dordrecht, The Netherlands: Springer, 2013, pp. 71–93.

[24] K. J. Parker, "Ultrasonic attenuation and absorption in liver tissue," *Ultrasound Med. Biol.*, vol. 9, no. 4, pp. 363–369, 1983.

[25] A. M. Pirmoazen, A. Khurana, A. El Kaffas, and A. Kamaya, "Quantitative ultrasound approaches for diagnosis and monitoring hepatic steatosis in nonalcoholic fatty liver disease," *Theranostics*, vol. 10, no. 9, pp. 4277–4289, 2020.

[26] L. Castera, V. Vilgrain, and P. Angulo, "Noninvasive evaluation of NAFLD," *Nature Rev. Gastroenterol. Hepatol.*, vol. 10, no. 11, pp. 666–675, Nov. 2013.

[27] O. W. Hamer, D. A. Aguirre, G. Casola, J. E. Lavine, M. Woenckhaus, and C. B. Sirlin, "Fatty liver: Imaging patterns and pitfalls," *RadioGraphics*, vol. 26, no. 6, pp. 1637–1653, Nov. 2006.

[28] F. M. Hooi, O. Kripfgans, and P. L. Carson, "Acoustic attenuation imaging of tissue bulk properties with a priori information," *J. Acoust. Soc. Amer.*, vol. 140, no. 3, p. 2113, Sep. 2016.

[29] A. D. Pawlicki and W. D. O'Brien, Jr., "Method for estimating total attenuation from a spatial map of attenuation slope for quantitative ultrasound imaging," *Ultrason. Imag.*, vol. 35, no. 2, pp. 162–172, 2013.

[30] D. M. Brandner et al., "Estimation of tissue attenuation from ultrasonic B-mode images—Spectral-log-difference and method-of-moments algorithms compared," *Sensors*, vol. 21, no. 7, p. 2548, Apr. 2021.

[31] F. Destrempes, M. Gesnik, and G. Cloutier, "Construction of adaptively regularized parametric maps for quantitative ultrasound imaging," in *Proc. IEEE Int. Ultrason. Symp. (IUS)*, Oct. 2019, pp. 2027–2030.

[32] H. Kim and T. Varghese, "Hybrid spectral domain method for attenuation slope estimation," *Ultrasound Med. Biol.*, vol. 34, no. 11, pp. 1808–1819, Nov. 2008.

[33] M. L. Oelze and J. Mamou, "Review of quantitative ultrasound: Envelope statistics and backscatter coefficient imaging and contributions to diagnostic ultrasound," *IEEE Trans. Ultrason., Ferroelectr., Freq. Control*, vol. 63, no. 2, pp. 336–351, Feb. 2016.

[34] A. L. Coila and R. Lavarello, "Regularized spectral log difference technique for ultrasonic attenuation imaging," *IEEE Trans. Ultrason., Ferroelectr., Freq. Control*, vol. 65, no. 3, pp. 378–389, Mar. 2018.

[35] F. Deeba et al., "SWTV-ACE: Spatially weighted regularization based attenuation coefficient estimation method for hepatic steatosis detection," in *Medical Image Computing and Computer Assisted Intervention–(MICCAI)*. Cham, Switzerland: Springer, 2019, pp. 610–618.

[36] R. Kuc and M. Schwartz, "Estimating the acoustic attenuation coefficient slope for liver from reflected ultrasound signals," *IEEE Trans. Sonics Ultrason.*, vol. SU-26, no. 5, pp. 353–361, Sep. 1979.

[37] J. Ophir et al., "Attenuation estimation in reflection: Progress and prospects," *Ultrason. Imag.*, vol. 6, no. 4, pp. 95–349, Oct. 1984.

[38] M. Insana, J. Zagzebski, and E. Madsen, "Improvements in the spectral difference method for measuring ultrasonic attenuation," *Ultrason. Imag.*, vol. 5, no. 4, pp. 331–345, Oct. 1983.

[39] K. J. Parker and R. C. Waag, "Measurement of ultrasonic attenuation within regions selected from B-scan images," *IEEE Trans. Biomed. Eng.*, vol. BME-30, no. 8, pp. 431–437, Aug. 1983.

[40] K. Samimi and T. Varghese, "Performance evaluation of the spectral centroid downshift method for attenuation estimation," *IEEE Trans. Ultrason., Ferroelectr., Freq. Control*, vol. 62, no. 5, pp. 871–880, May 2015.

[41] K. Nam, I. M. Rosado-Mendez, N. C. Rubert, E. L. Madsen, J. A. Zagzebski, and T. J. Hall, "Ultrasound attenuation measurements using a reference phantom with sound speed mismatch," *Ultrason. Imag.*, vol. 33, no. 4, pp. 251–263, 2011.

[42] P. Gong, P. Song, C. Huang, J. Trzasko, and S. Chen, "System-independent ultrasound attenuation coefficient estimation using spectra normalization," *IEEE Trans. Ultrason., Ferroelectr., Freq. Control*, vol. 66, no. 5, pp. 867–875, May 2019.

[43] I. Rafati, F. Destrempes, and G. Cloutier, "Regularized phantom-free construction of local attenuation coefficient slope maps for quantitative ultrasound imaging," in *Proc. IEEE Int. Ultrason. Symp. (IUS)*, Sep. 2020, pp. 1–3.

[44] I. M. Rosado-Mendez et al., "Task-oriented comparison of power spectral density estimation methods for quantifying acoustic attenuation in diagnostic ultrasound using a reference phantom method," *Ultrason. Imag.*, vol. 35, no. 3, pp. 34–214, Jul. 2013.

[45] M. A. Fischler and R. Bolles, "Random sample consensus: A paradigm for model fitting with applications to image analysis and automated cartography," *Commun. ACM*, vol. 24, no. 6, pp. 381–395, 1981.

[46] L. Yazdani, M. Bhatt, I. Rafati, A. Tang, and G. Cloutier, "The revisited frequency-shift method for shear wave attenuation computation and imaging," *IEEE Trans. Ultrason., Ferroelectr., Freq. Control*, vol. 69, no. 6, pp. 2061–2074, Jun. 2022.

[47] D. J. Sheskin, *Handbook of Parametric and Nonparametric Statistical Procedures*, 5th ed. Boca Raton, FL, USA: CRC Press, 2011.

[48] R. J. Tibshirani and J. Taylor, "The solution path of the generalized LASSO," *Ann. Statist.*, vol. 39, no. 3, pp. 1335–1371, Jun. 2011.

[49] A. Kolmogorov, "Sulla determinazione empirica di una lgge di distribuzione," *Giornale dell'Istituto Italiano degli Attuari*, vol. 4, pp. 83–91, Aug. 1933.

[50] P. M. Shankar, "A general statistical model for ultrasonic backscattering from tissues," *IEEE Trans. Ultrason., Ferroelectr., Freq. Control*, vol. 47, no. 3, pp. 727–736, May 2000.

[51] G. Schwarz, "Estimating the dimension of a model," *Ann. Statist.*, vol. 6, no. 2, pp. 461–464, Jan. 1978.

[52] E. L. Madsen, J. A. Zagzebski, R. A. Banjavie, and R. E. Jutila, "Tissue mimicking materials for ultrasound phantoms," *Med. Phys.*, vol. 5, no. 5, pp. 391–394, Sep. 1978.

[53] D. Garcia, L. Le Tarnec, S. Muth, E. Montagnon, J. Porée, and G. Cloutier, "Stolt's f-k migration for plane wave ultrasound imaging," *IEEE Trans. Ultrason., Ferroelectr., Freq. Control*, vol. 60, no. 9, pp. 1853–1867, Sep. 2013.

[54] A. Tang et al., "Nonalcoholic fatty liver disease: MR imaging of liver proton density fat fraction to assess hepatic steatosis," *Radiology*, vol. 267, no. 2, pp. 31–422, May 2013.

[55] A. Tang et al., "Accuracy of MR imaging–estimated proton density fat fraction for classification of dichotomized histologic steatosis grades in nonalcoholic fatty liver disease," *Radiology*, vol. 274, no. 2, pp. 416–425, Feb. 2015.

[56] R. P. Carbente, J. M. Maia, and A. A. Assef, "Image reconstruction utilizing median filtering applied to elastography," *Biomed. Eng. OnLine*, vol. 18, no. 1, p. 22, Mar. 2019.

[57] J. S. Paige et al., "A pilot comparative study of quantitative ultrasound, conventional ultrasound, and MRI for predicting histology-determined steatosis grade in adult nonalcoholic fatty liver disease," *Amer. J. Roentgenol.*, vol. 208, no. 5, pp. 168–177, May 2017.

[58] Y. Y. Liao et al., "Multifeature analysis of an ultrasound quantitative diagnostic index for classifying nonalcoholic fatty liver disease," *Sci. Rep.*, vol. 6, p. 35083, Oct. 2016.
[59] T. Tada et al., "Usefulness of attenuation imaging with an ultrasound scanner for the evaluation of hepatic steatosis," *Ultrasound Med. Biol.*, vol. 45, no. 10, pp. 2679–2687, Oct. 2019.
[60] T. Tada et al., "Utility of attenuation coefficient measurement using an ultrasound-guided attenuation parameter for evaluation of hepatic steatosis: Comparison with MRI-determined proton density fat fraction," *Amer. J. Roentgenol.*, vol. 212, no. 2, pp. 332–341, Feb. 2019.
[61] K. Imajo et al., "Utility of ultrasound-guided attenuation parameter for grading steatosis with reference to MRI-PDFF in a large cohort," *Clin. Gastroenterol. Hepatol.*, vol. 21, pp. 1182–1184, Nov. 2021.
[62] V. Barrere, M. Sanchez, S. Cambronero, A. Dupré, M. Rivoire, and D. Melodelima, "Evaluation of ultrasonic attenuation in primary and secondary human liver tumors and its potential effect on high-intensity focused ultrasound treatment," *Ultrasound Med. Biol.*, vol. 47, no. 7, pp. 1761–1774, Jul. 2021.
[63] B. Carpentier, J. Hayward, and L. Strachowski, "Enhancing your acoustics: Ultrasound image optimization of breast lesions," *J. Ultrasound Med.*, vol. 36, no. 7, pp. 1479–1485, Jul. 2017.
[64] N. Jafarpisheh, T. J. Hall, H. Rivaz, and I. M. Rosado-Mendez, "Analytic global regularized backscatter quantitative ultrasound," *IEEE Trans. Ultrason., Ferroelectr., Freq. Control*, vol. 68, no. 5, pp. 1605–1617, May 2021.
[65] K. A. Wear, "A Gaussian framework for modeling effects of frequency-dependent attenuation, frequency-dependent scattering, and gating," *IEEE Trans. Ultrason., Ferroelectr., Freq. Control*, vol. 49, no. 11, pp. 1572–1582, Nov. 2002.
[66] M. Hassannejad Bibalan and H. Amindavar, "Non-Gaussian amplitude PDF modeling of ultrasound images based on a novel generalized cauchy-Rayleigh mixture," *EURASIP J. Image Video Process.*, vol. 2016, no. 1, p. 48, Dec. 2016.
[67] P. Gong et al., "Noise suppression for ultrasound attenuation coefficient estimation based on spectrum normalization," *IEEE Trans. Ultrason., Ferroelectr., Freq. Control*, vol. 68, no. 8, pp. 2667–2674, Aug. 2021.

Iman Rafati received the bachelor's degree in computational engineering sciences and the master's degree in biomedical engineering from the University of Tehran, Tehran, Iran, in 2014 and 2016, respectively. He is currently pursuing the Ph.D. degree in biomedical engineering with the Université de Montréal, Montreal, QC, Canada.

His current research interests are quantitative ultrasound (QUS) imaging, elastography, and liver cancer diagnosis by QUS.

François Destrempes received the B.Sc. degree in mathematics from the Université de Montréal, Montreal, QC, Canada, in 1985, the Ph.D. degree in mathematics from Cornell University, Ithaca, NY, USA, in 1990, and the Ph.D. degree in computer science from the Université de Montréal in 2006.

Since 2008, he has been a Research Associate with the Laboratory of Biorheology and Medical Ultrasonics, Centre de recherche du Centre Hospitalier de l'Université de Montréal, Montreal. He has authored or coauthored 45 articles and two book chapters. His current research interests include ultrasound imaging, segmentation of ultrasound images, quantitative ultrasound, and machine learning applied to medical imaging.

Ladan Yazdani received the B.Sc. degree in electrical engineering with a minor in biomedical engineering and the M.Sc. degree in biomedical engineering from the University of Tehran, Tehran, Iran, in 2015 and 2018, respectively. She is currently pursuing the Ph.D. degree in biomedical engineering with the Université de Montréal, Montreal, QC, Canada.

She joined the Laboratory of Biorheology and Medical Ultrasonics, Centre de recherche du Centre Hospitalier de l'Université de Montréal, Montreal, in 2019. Her current research interests include ultrasound imaging, ultrasound elastography, and liver disease diagnosis by ultrasound.

Marc Gesnik received the Engineering degree from the École Supérieure de Physique et de Chimie Industrielles de la Ville de Paris (ESPCI Paris), Paris, France, in 2014, the M.Sc. degree in physical acoustics from Paris VII University, Paris, in 2014, and the Ph.D. degree from the Institut Langevin, Centre National de la Recherche Scientifique (CNRS), Institut National de la Santé et de la Recherche Médicale (INSERM), ESPCI Paris, in 2017.

He was a Postdoctoral Fellow with the Centre de recherche du Centre Hospitalier de l'Université de Montréal, Montreal, QC, Canada. He is currently working at Iconeus Company, Paris. His research interests include elastography, quantitative ultrasound imaging, functional ultrasound imaging, and photoacoustics.

An Tang received the M.D. degree from the University of Sherbrooke, Sherbrooke, QC, Canada, in 2000.

He completed his radiology residency at the Université de Montréal, Montreal, QC, Canada, in 2005. He pursued fellowship training in abdominal imaging at the University of Toronto, Toronto, ON, Canada, in 2006. He is currently a Clinical Scientist with the Centre hospitalier de l'Université de Montréal, Montreal, a Senior Research Scholar with the Fonds de recherche du Québec—Santé (FRQS), Montreal, and a Professor of radiology with the Université de Montréal. His research interests focus on imaging-based techniques for the diagnosis and monitoring of chronic liver disease and liver cancer.

Guy Cloutier (Senior Member, IEEE) is currently the Director of the Laboratory of Biorheology and Medical Ultrasonics, University of Montreal Hospital Research Centre, Montreal, QC, Canada, and a Professor with the Department of Radiology, Radiation Oncology, and Nuclear Medicine and the Institute of Biomedical Engineering, Université de Montréal, Montreal. He has authored more than 230 peer-reviewed articles and has several patents and licensed four technologies. His research interests are quantitative ultrasound imaging, quasi-static and dynamic ultrasound elastography, the development of multiphysics imaging methods, and biomechanical modeling.

Dr. Cloutier was a recipient of the National Scientist Award of the Fonds de la Recherche en Santé du Québec.